Identifying embedded accreting protoplanets at and within the diffraction limit using photonic lantern spectro-astrometry

Daniel M. Levinstein[a], Stephanie Sallum[a], Yoo Jung Kim[b], Jonathan Lin[b], Nemanja Jovanovic[c], Michael P. Fitzgerald[b], Yinzi Xin[c], Olivier Guyon[d,e], Barnaby Norris[f], Christopher Betters[g], Sergio Leon-Saval[g], Vincent Deo[d], Julien Lozi[d], Sébastien Vievard[d], and Kyohoon Ahn[d,h]

[a]Department of Physics and Astronomy, 4129 Frederick Reines Hall, University of California Irvine, Irvine, CA 92697
[b]UCLA Physics & Astronomy, 475 Portola Plaza, Los Angeles, CA 90095-1547
[c]Department of Astronomy, California Institute of Technology, Pasadena, CA 91125, USA
[d]National Astronomical Observatory of Japan, Subaru Telescope, 650 North Aohoku Place, Hilo, HI 96720, USA
[e]The University of Arizona, Department of Astronomy and Steward Observatory, 933 N. Cherry Ave., Tucson, AZ 85719, USA
[f]The University of Sydney, Sydney Institute for Astronomy, Physics Road, Sydney, NSW 2006, Australia
[g]The University of Sydney, Sydney Astrophotonic Instrumentation Laboratory, Sydney, NSW 2006, Australia
[h]Korea Astronomy and Space Science Institute, 776 Daedeok-daero, Yuseong District, Daejeon, South Korea

ABSTRACT

Innovation in high angular resolution imaging is essential to identifying planet formation on solar-system scales ($\sim 5-10$ AU) in active star forming regions beyond 150 pc. The photonic lantern is a novel fiber-optic device that can be used to overcome the observational challenges associated with imaging such close-in protoplanets. Photonic lanterns spatially filter out modal noise with high throughput and low power loss, making them appealing for a wide variety of applications including wavefront-sensing, nulling, and spectro-astrometry. Spectro-astrometry, a technique that identifies wavelength-dependent centroid shifts in spectrally-dispersed datasets, could enable the resolution of circumstellar structures within the diffraction limit when conducted with photonic lanterns. Here, we present simulations of spectro-astrometric observations of embedded protoplanets using photonic lanterns. We generate mock, 6-port photonic lantern observations of young stars with gapped circumstellar disks containing accreting protoplanets with emission at the Paschen β hydrogen line. The simulations assume a 10-m class telescope and realistic sources of both photon noise and residual adaptive optics errors. We demonstrate the detection of protoplanets with photonic lantern spectro-astrometry in the presence of circumstellar material by constraining planetary accretion characteristics such as planet separation, position angle, and stellar contrast, and we explore the biases introduced by the presence of the circumstellar material.

1. INTRODUCTION

Recent exoplanet discoveries have found several planetary mass companions (PMCs) embedded within circumstellar disks, providing insight into how disk-star and disk-planet interactions impact the earliest stages of planet formation. PDS 70 is one such system which has two planetary companions, one embedded in its circumstellar disk at $\sim$ 38 au ($\sim$ 230 mas) and another residing in a disk clearing at $\sim$ 22 au ($\sim$ 180 mas).[1,2] Both of these PMCs were detected from their IR continuum emission and later solidified as protoplanets due to their Hα emission which is not present in the surrounding disk environment. Similarly, MWC 758 c is located at a

Optical and Infrared Interferometry and Imaging IX, edited by Jens Kammerer, Stephanie Sallum, Joel Sanchez-Bermudez, Proc. of SPIE Vol. 13095, 130952M
 · 0277-786X · doi: 10.1117/12.3019296

separation of ~ 97 au (~ 620 mas) in the spiral arms of a protoplanetary disk and was detected by its distinct infrared spectral features reminiscent of a large red planet.[3] The discovery of these planets, in addition to many others, marks the beginning of a trend toward broadening our understanding of early stage planet formation, and the influence of stellar and dynamical disk effects on this process. Further, focusing this exploration of early planet formation at orbital scales similar to our own Solar System giants will deepen our comprehension of its formation billions of years ago. Emerging high spectral-resolution imaging methods, alongside established high spatial-resolution imaging techniques, will help illuminate early stage planet formation in extrasolar planetary systems.

Current instrumentation and detection methods have proven sufficient to find wide orbit accreting protoplanets, but they are less effective at identifying accreting PMCs orbiting on the scale of our Solar System giants, especially within Jupiter's orbit. The nearest active star-forming regions in the local group can be found around 150 pc.[4,5] At this distance, a forming planet with a separation similar to that of Jupiter (~ 5 AU) would have an angular separation of ~ 33 mas viewed from Earth. On a 10m class telecscope, this is within the diffraction limit for IR continuum ($2-4\mu$m) and nearly the diffraction limit for Paschen β (Paβ, 1.282μm), rendering the search for these planets exceedingly difficult with traditional imaging methods even with perfect adaptive optics (AO) correction.[6] Deploying new techniques and instrumentation, such as combining the centroiding capabilities of spectro-astrometry[7] with the low-noise and high-throughput of photonic lanterns, will allow us to overcome these limitations by enabling sub-diffraction-limited observations of planets in their earliest stages.

Spectro-astrometry (SA) utilizes the spatially-resolved spectrum of a known object to identify wavelength-dependent centroid shifts within the diffraction limit.[7] For example, given an unresolved binary consisting of a bright star with a continuous spectrum and a dimmer star with an emission line at some wavelength λ_0, SA will find the centroid of the binary as a function of wavelength. The centroid will be on the bright star at any wavelength other than λ_0, but the centroid at λ_0 will shift toward the fainter star with the emission feature. This centroid shift indicates that the system is actually a binary.[7,8] Although the binary is unresolved with traditional imaging, SA can infer the presence of multiple objects within the diffraction limit. SA of accreting protoplanets works similarly to binaries, however the planet is generally far dimmer, shrouded by circumstellar material, and emits at specific wavelengths such as Hα (0.656μm), Brγ (2.166μm), and Paβ (1.282μm).[9] SA of protoplanets at and below the diffraction limit is especially difficult without high-contrast instrumentation due to the dim nature of the sources and the residual aberrations present in AO-corrected light.[8]

The application of SA with photonic lanterns would provide the high throughput and spatial-filtering required to detect protoplanets at these angular separations. Photonic lanterns are optical devices that consist of a large multi-mode fiber input that transitions adiabatically into several single-mode fiber outputs.[10] By themselves, single-mode fibers filter out higher order linear polarization modal noise from injected signals, yielding clear Gaussian shaped point spread functions. However, due to their size, they have very limited throughput resulting in sub-optimal efficacy on dim sources. By accepting higher order linear polarization modes, multi-mode fibers take in much more light than single mode fibers, allowing for dimmer sources to be viewed. Yet, this combination of different linear polarizations of light produces a much noisier overall signal.[10] Transitioning to single mode outputs combines the benefits of both types of fibers, resulting in a stable, low-modal-noise, high-throughput device which, when combined with the technique of SA, is ideal for detecting high contrast sources such as accreting protoplanets.

We present numerical simulations of spectro-astrometry with photonic lanterns to recover injected parameters of an accreting protoplanet in the presence of a circumstellar disk using a Markov chain Monte Carlo (MCMC) algorithm.[11] The models consist of three parameters defining brightness, separation, and position angle of an accreting protoplanet in addition to parameters detailing the shape, size, brightness, and position angle of the circumstellar disk. Photon noise and Zernike tip-tilt jitter representing adaptive optics errors are included to simulate a realistic noisy observation. In Section 2, we describe the methods used to simulate spectro-astrometry with a 6 port photonic lantern. In Section 3 we present results of the recovered protoplanet parameters and discuss the fit to the injected model. Finally, we summarize our results in Section 4.

2. METHODS

2.1 Protoplanet and Circumstellar Disk Model

We generate geometric models consisting of a central point source representing a star and another point source representing an accreting protoplanet defined by angular separation, position angle on sky, and integrated contrast relative to the star. A Gaussian circumstellar disk is also added, defined by a major axis radius, radial and azimuthal FWHM, major-to-minor axis ratio, and major axis position angle on sky. The accreting protoplanet brightness depends on the wavelength along a hydrogen line profile centered at Paβ, shown in Figure 1. The intensity value at each wavelength on this profile scales the protoplanet brightness in the model image. The assumed planetary infall rate FWHM of 100 km/s is the expected free-fall velocity onto an accreting giant protoplanet assuming a planetary mass of 5 M_J and radius 1.6 R_J. The star is represented by a blackbody spectrum with an effective temperature of 6550 K, radius of 1.882 $R_\odot$, and luminosity of 5.87 $L_\odot$ at a distance of 150 pc.

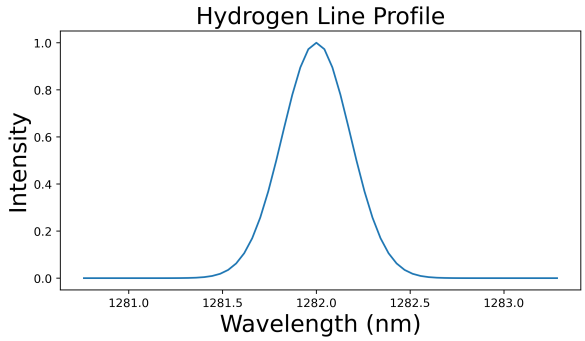

Figure 1. Accreting protoplanet hydrogen line profile centered on Paβ emission line. The profile has a FWHM corresponding to an infall velocity of ~ 100 km/s, and a sampling corresponding to a spectrograph resolving power of $R \approx 30000$.

2.2 Photonic Lantern Simulation

Assuming small optical aberrations, propagation of light in a PL is linear so the input complex-valued electric field $\boldsymbol{u}_{in}$ is directly related to the output electric field $\boldsymbol{u}_{out}$ and the intensity response $\boldsymbol{p}_{out}$. We utilized a monochromatic transfer matrix $\mathbf{A}$ at Paβ to simulate a standard 6 port PL.[8,12,13] Figure 2 represents the six complex-valued modes of the transfer matrix $\mathbf{A}$ in both the pupil and focal planes. Equation 1 describes the propagation of light through the lantern to the PL output ports as a complex-valued electric field and real-valued intensities. We use the same PL transfer matrix for all wavelengths from 1.281 - 1.283 μm as the propagation of light in this sufficiently small range is nearly constant as a function of wavelength. The Fourier transform of the input model is multiplied by the simulated 10-m telescope aperture from HCIPy[14] to obtain the input electric field. Plugging $\boldsymbol{u}_{in}$ into 1b yields the intensity response when combined with the transfer matrix $\mathbf{A}$.

$$\boldsymbol{u}_{out} = \mathbf{A}\boldsymbol{u}_{in} \tag{1a}$$

$$\boldsymbol{p}_{out} = |\mathbf{A}\boldsymbol{u}_{in}|^2 \tag{1b}$$

2.3 Simulated Noisy Observations

We generated models at wavelengths from 1280.76 nm to 1283.28 nm with $\Delta\lambda = 0.043$, or R $\approx$ 30000. Using these models, we simulated observations assuming a total integration time of 2 hours split into 360 20-second exposures. Each exposure has 20000 layers of tip/tilt jitter from a normal distribution with $\sigma = 0.5$ radians applied to the pupil plane image to emulate residual adaptive optics errors with a Strehl ratio of 0.62 at J band.[15] We added photon noise to each PL output port intensity using a Poisson distribution defined by the telescope collecting area, and stellar brightness, and photon count in each port. We calculate the effective PL signal as the mean of the 360 simulated exposures with error bars defined by the standard error of the exposures.

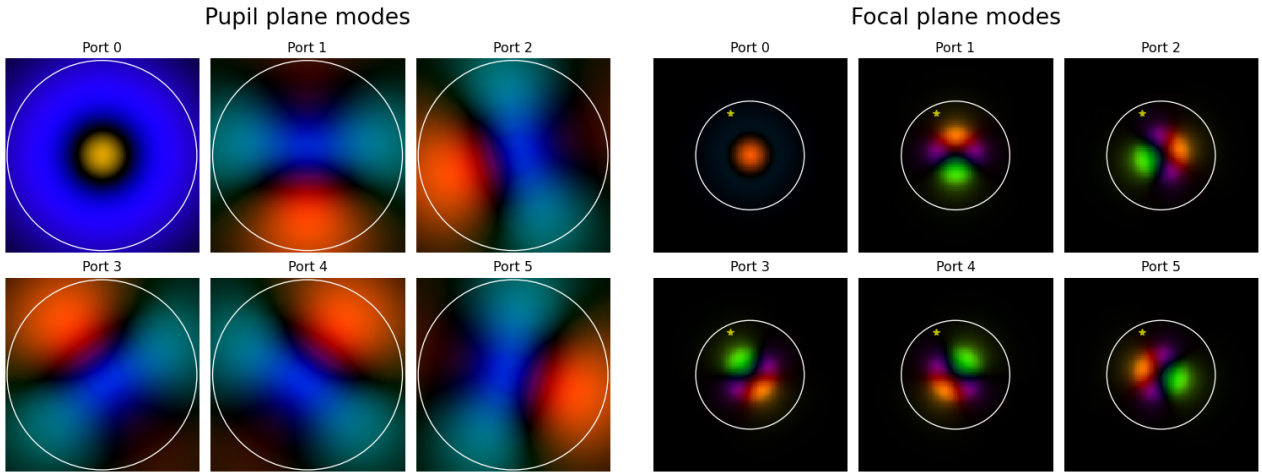

Figure 2. Left: Individual panels depict the complex pupil plane linear-polarization supermodes of each photonic lantern port. The color scale indicates phase differences in the complex electric field and the circle represents the telescope aperture of 10 m in diameter. Right: These panels depict the complex focal plane supermodes in each port. The white circle represents the extent of the multi-mode input with a radius of 33.6 mas. The gold star illustrates the location of the planet on the photonic lantern.

2.4 Protoplanet Recovery with Markov chain Monte Carlo

We use a parallel tempered Markov chain Monte Carlo python package `PTMCMCSampler`[11] to recover protoplanet parameters from the simulated observations. We utilize a differential measurement with respect to the average intensity away fromThe algorithm searches the parameter space of the three protoplanet variables outlined in Section 2.1. With each set of values for the three parameters, a binary model is constructed and the log-likelihood is calculated as $-0.5 * \chi^2$, where χ^2 is the measured goodness of fit of the model and the simulated observation. The χ^2 goodness of fit is calculated by comparing the wavelength dependent changes in intensity normalized by the average intensity away from the Paβ line. The best fit model is the mean of the distribution of each parameter's chain, as shown in Figure 3. The error bars are the 1-sigma standard deviation from the mean, or the range between the 16th and 84th percentiles of the samples.

3. RESULTS AND DISCUSSION

Table 1 lists the injected disk and protoplanet parameters alongside the recovered protoplanet parameters. The corner plots in Figure 3 show the convergence of MCMC to the best fit protoplanet parameters after 10000 steps, in addition to the injected parameters in red for simulated observations with and without a circumstellar disk. For the simulated observation containing a circumstellar disk, the recovered planet separation is $29.23^{+0.83}_{-0.86}$ mas, within one standard deviation of the injected value. The position angle (E of N) is also within one standard deviation with a recovered value of $24.18^{+1.55}_{-1.69}$ degrees. The protoplanet contrast is biased and disagrees with the injected value (0.01) by greater than 5σ, with a recovered value of $0.00786^{+0.00004}_{-0.00003}$. For the model without a disk, both the planet separation and position angle converge to within 1σ, with values of $28.91^{+0.98}_{-0.81}$ mas and $24.19^{+1.81}_{-1.73}$ degrees, respectively. The protoplanet contrast exhibits a similar but smaller bias compared to the disk model, converging to a value of $0.00817^{+0.00004}_{-0.00004}$.

The model reconstruction shown in Figure 4 shows the recovered protoplanet at a similar location relative to the star as in the injected disk model, as well as the difference of the injected and recovered models. There is only one point in the difference image representing the protoplanet location indicating good spatial recovery with the recovered protoplanet at the same pixel as the injected protoplanet. The residual brightness in the difference plot is due to the higher recovered protoplanet contrast as seen in Table 1.

The relative intensities from Figure 5 show the simulated observation (black error bars) along with various models. Ports 1 and 3 exhibit very good agreement between the observations and the best-fit model (orange

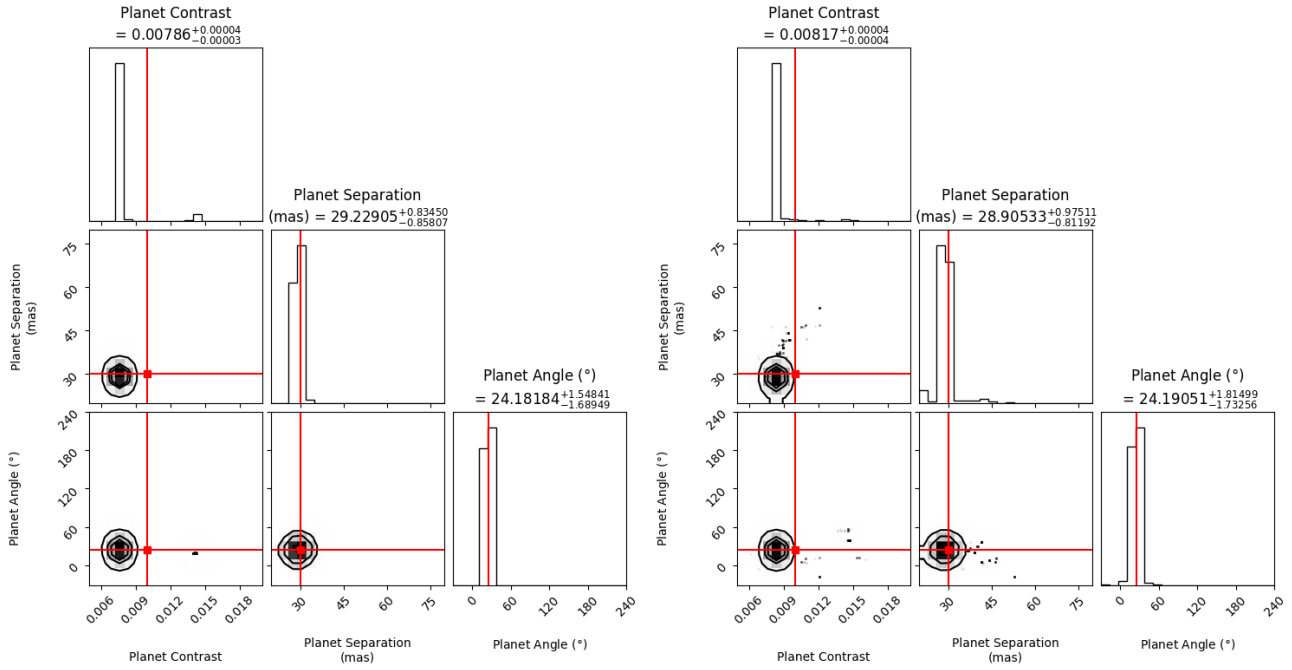

Figure 3. Corner plots showing the convergence of MCMC after 10000 steps for an injected signal including a circumstellar disk (left) and without a disk (right). Planet angle and separation agree with the injected value to within 1σ. Planet contrast is systematically higher at $> 5\sigma$.

Model	Disk		No Disk	
Parameter	Injected Value	Recovered Value	Injected Value	Recovered Value
Protoplanet Contrast	0.01	$0.00786^{+0.00004}_{-0.00003}$	0.01	$0.00817^{+0.00004}_{-0.00004}$
Planet Separation (mas)	30	$29.23^{+0.83}_{-0.86}$	30	$28.91^{+0.98}_{-0.81}$
Planet Position Angle (°)	25	$24.18^{+1.55}_{-1.69}$	25	$24.19^{+1.81}_{-1.73}$
Disk Contrast	0.1	–	–	–
Axis Ratio	0.6	–	–	–
Major Axis Radius (mas)	100	–	–	–
Disk Position Angle (°)	116	–	–	–
Radial σ (mas)	50	–	–	–
Azimuthal σ (°)	201	–	–	–

Table 1. Injected and recovered parameters for simulated observations of embedded protoplanets. We only fit the protoplanet parameters, so there are no recovered values for the disk parameters.

line). Ports 0 and 4 have middling agreement at the Paβ line, and Ports 2 and 5 have relatively weak agreement with the simulated observation. The intensity in each port is dependent on the alignment of the injected signal with the lantern in the focal plane.[10] Due to normalizing the outputs of the photonic lantern, we expect the highest relative intensity change to be associated with the port(s) closest to the protoplanet. Our simulations show that this occurs as expected in port 3, the port geometrically closest to the protoplanet (seen in Figure 2). This port drives the fit because the signal-to-noise there is maximized, the contribution to the log-likelihood is maximized, and thus the recovered model most closely matches this data. The other ports, especially port 2, have much smaller impacts on the log-likelihood and as a result they are less favored in the fit. The star and protoplanet model cannot fit to all ports simultaneously due to systematic effects that we discuss in the following paragraphs.

Unlike the location parameters, the protoplanet contrast converges to a value much further from the injected signal, at around 5σ from the injected value. This discrepancy is illustrated in both models in Figure 5. The

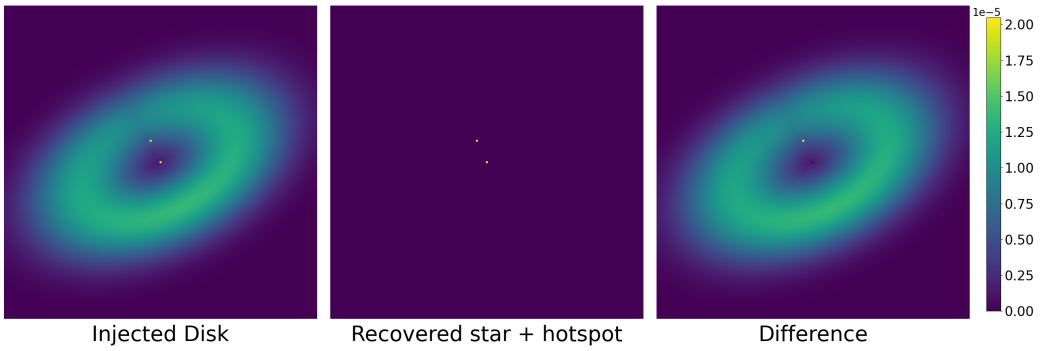

Figure 4. Injected, recovered, and difference images for the simulated observation. The recovered protoplanet location is in the same location as the injected location. The shared color bar indicates brightness relative to the star, with a max brightness set low enough to show the disk in the injected scene. The difference image shows a good fit to the protoplanet location with a brightness difference visible in the residual image.

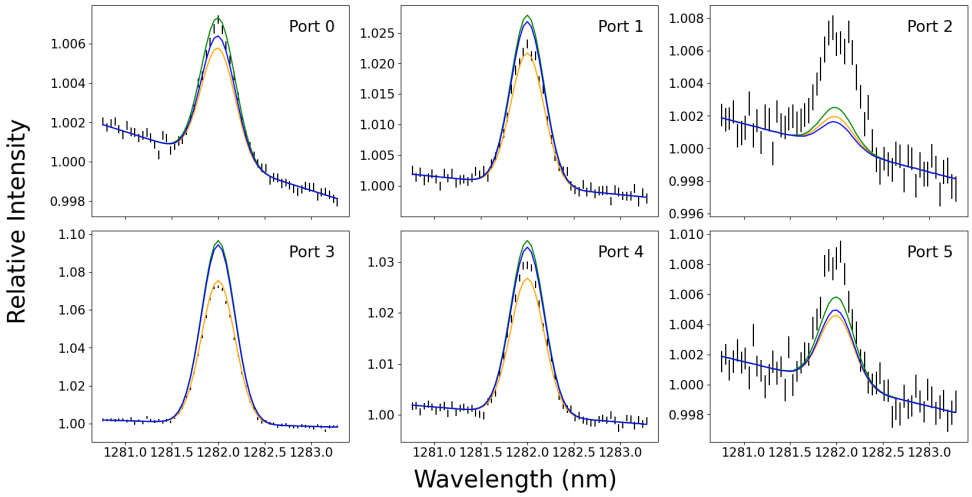

Figure 5. Lantern outputs as a function of wavelength, with each panel showing the output of a single port. The signal from the noiseless injected disk scene is shown in blue, the injected star and planet only is shown in green, the recovered model in orange, and the simulated five hour observation is represented by the black error bars. The excess flux around 1.28 microns in each plot is due to the protoplanet accretion signature at Paβ.

green lines in Figure 5 show noiseless intensities for a model consisting of just the central star and the protoplanet without a disk, to illustrate a perfect recovery of the protoplanet at the injected contrast. The blue lines represent a noiseless model of the disk and planet to demonstrate an observation without photon noise or residual AO errors. As evidenced by the mismatch between these lines and the black error bars, both of these models exhibit systematic offsets introduced by the addition of noise. Ports 2, 3, and 5 demonstrate this bias most clearly, wherein the simulated observation has a considerable decrease in relative flux in port 3 and an increase in ports 2 and 5 compared to the noiseless models in blue and green. One of the main drivers of this relative flux shift is a blurring effect caused by the simulated AO errors. The tip/tilt jitter added to simulate AO residual errors effectively blurs the injected model, causing the flux at each location to spread to nearby ports. Observers traditionally fit a planet using a point source, so the systematic biases introduced by the residual AO errors cause the fit to converge to a higher contrast planet.

Comparing the recovered contrasts for the simulated observations with and without a disk, we see a further increase in contrast for the observation with a disk. The relative change in flux is dependent on the normalization of the counts in each port away from Paβ. In the presence of a disk, the light from the disk increases flux in each port at all wavelengths. Normalizing the signals in each port produces a lower relative flux at Paβ with a

disk present than without. As a result, since we only fit a star and protoplanet to the injected signal, a higher planet contrast is favored.

Both corner plots in Figure 3 show good convergence to the injected parameters defining the planet's location. Both with and without the disk, we are able to constrain the location of an embedded accreting companion near the diffraction limit to within 1σ of the injected value. Despite the systematic errors in contrast, localizing this signal demonstrates that PLs could potentially be used to isolate embedded protoplanets with realistic luminosities. For example, given an injected contrast of 5 mag, the line luminosity at Paβ is $6.09 \times 10^{-6} L_{\odot}$ and the accretion luminosity is calculated to be $L_{acc} = 0.005 L_{\odot}$.[9] This accretion luminosity yields $M_p \dot{M} \sim 3.6 \times 10^{-5} \mathrm{M_J^2 yr^{-1}}$, assuming a L_{acc}-$M_p\dot{M}$ relationship similar to low-mass accreting T Tauri stars and a planetary radius of $1.6 \mathrm{R_J}$.[16] This planet mass times accretion rate is roughly consistent with expectations for runaway growth.

4. CONCLUSION

Spectro-astrometry with photonic lanterns is an emerging technique for detecting planet formation on solar system scales. Our numerical simulations of a 6-port photonic lantern demonstrate the ability to recover the location of an injected accreting protoplanet within one standard devation using MCMC. This method also constrains the injected protoplanet brightness to within 20% of the injected value in the presence of disk emission and other systematic offsets. The next step is to vary the protoplanet location and brightness and explore the limitations of this method of parameter recovery, namely the highest detectable contrast and closest detectable separation. We will also explore the efficacy of recovery with different amounts of tip/tilt jitter and expand this technique to photonic lanters with more ports. The ability to localize and constrain the contrast of an accreting companion near the diffraction limit reveals the potential of this technology to shed light on earlier stages of planet formation than previously observed. Combining this technique with future extreme AO facilities could potentially allow for protoplanet detection at separations similar to our inner Solar System.

ACKNOWLEDGMENTS

This work is supported by the National Science Foundation under Grant No. 2109231. Any opinions, findings, and conclusions or recommendations expressed in this material are those of the author(s) and do not necessarily reflect the views of the National Science Foundation.

REFERENCES

[1] Haffert, S. Y., Bohn, A. J., de Boer, J., Snellen, I. a. G., Brinchmann, J., Girard, J. H., Keller, C. U., and Bacon, R., "Two accreting protoplanets around the young star PDS 70," *Nature Astronomy* **3**, 749–754 (Aug. 2019).

[2] Keppler, M., Benisty, M., Müller, A., Henning, Th., Van Boekel, R., Cantalloube, F., Ginski, C., Van Holstein, R. G., Maire, A.-L., Pohl, A., Samland, M., Avenhaus, H., Baudino, J.-L., Boccaletti, A., De Boer, J., Bonnefoy, M., Chauvin, G., Desidera, S., Langlois, M., Lazzoni, C., Marleau, G.-D., Mordasini, C., Pawellek, N., Stolker, T., Vigan, A., Zurlo, A., Birnstiel, T., Brandner, W., Feldt, M., Flock, M., Girard, J., Gratton, R., Hagelberg, J., Isella, A., Janson, M., Juhasz, A., Kemmer, J., Kral, Q., Lagrange, A.-M., Launhardt, R., Matter, A., Ménard, F., Milli, J., Mollière, P., Olofsson, J., Pérez, L., Pinilla, P., Pinte, C., Quanz, S. P., Schmidt, T., Udry, S., Wahhaj, Z., Williams, J. P., Buenzli, E., Cudel, M., Dominik, C., Galicher, R., Kasper, M., Lannier, J., Mesa, D., Mouillet, D., Peretti, S., Perrot, C., Salter, G., Sissa, E., Wildi, F., Abe, L., Antichi, J., Augereau, J.-C., Baruffolo, A., Baudoz, P., Bazzon, A., Beuzit, J.-L., Blanchard, P., Brems, S. S., Buey, T., De Caprio, V., Carbillet, M., Carle, M., Cascone, E., Cheetham, A., Claudi, R., Costille, A., Delboulbé, A., Dohlen, K., Fantinel, D., Feautrier, P., Fusco, T., Giro, E., Gluck, L., Gry, C., Hubin, N., Hugot, E., Jaquet, M., Le Mignant, D., Llored, M., Madec, F., Magnard, Y., Martinez, P., Maurel, D., Meyer, M., Möller-Nilsson, O., Moulin, T., Mugnier, L., Origné, A., Pavlov, A., Perret, D., Petit, C., Pragt, J., Puget, P., Rabou, P., Ramos, J., Rigal, F., Rochat, S., Roelfsema, R., Rousset, G., Roux, A., Salasnich, B., Sauvage, J.-F., Sevin, A., Soenke, C., Stadler, E., Suarez, M., Turatto, M., and Weber, L., "Discovery of a planetary-mass companion within the gap of the transition disk around PDS 70," *Astronomy & Astrophysics* **617**, A44 (Sept. 2018).

[3] Wagner, K., Stone, J., Skemer, A., Ertel, S., Dong, R., Apai, D., Spalding, E., Leisenring, J., Sitko, M., Kratter, K., Barman, T., Marley, M., Miles, B., Boccaletti, A., Assani, K., Bayyari, A., Uyama, T., Woodward, C. E., Hinz, P., Briesemeister, Z., Lawson, K., Ménard, F., Pantin, E., Russell, R. W., Skrutskie, M., and Wisniewski, J., "Direct images and spectroscopy of a giant protoplanet driving spiral arms in MWC 758," *Nature Astronomy* **7**, 1208–1217 (Oct. 2023).

[4] Reipurth, B., [*Handbook of Star Forming Regions, Volume I: The Northern Sky*], vol. 4 (2008).

[5] Reipurth, B., [*Handbook of Star Forming Regions, Volume II: The Southern Sky*], vol. 5 (2008).

[6] Guyon, O., Eisner, J. A., Angel, R., Woolf, N. J., Bendek, E. A., Milster, T. D., Ammons, S. M., Shao, M., Shaklan, S., Levine, M., Nemati, B., Martinache, F., Pitman, J., Woodruff, R. A., and Belikov, R., "SIMULTANEOUS EXOPLANET CHARACTERIZATION AND DEEP WIDE-FIELD IMAGING WITH A DIFFRACTIVE PUPIL telESCOPE," *The Astrophysical Journal* **767**, 11 (Mar. 2013).

[7] Whelan, E. and Garcia, P., "Spectro-astrometry: The method, its limitations, and applications," in [*Jets from Young Stars II*], Bacciotti, F., Testi, L., and Whelan, E., eds., **742**, 123 (2008).

[8] Kim, Y. J., Sallum, S., Lin, J., Xin, Y., Norris, B., Betters, C., Leon-Saval, S., Lozi, J., Vievard, S., Gatkine, P., Guyon, O., Jovanovic, N., Mawet, D., and Fitzgerald, M. P., "Spectroastrometry with photonic lanterns," in [*Ground-Based and Airborne Instrumentation for Astronomy IX*], **12184**, 1391–1402, SPIE (Aug. 2022).

[9] Aoyama, Y., Marleau, G.-D., Ikoma, M., and Mordasini, C., "Comparison of Planetary Hα-emission Models: A New Correlation with Accretion Luminosity," *The Astrophysical Journal Letters* **917**, L30 (Aug. 2021).

[10] Leon-Saval, S. G., Argyros, A., and Bland-Hawthorn, J., "Photonic lanterns," *Nanophotonics* **2**, 429–440 (Dec. 2013).

[11] Ellis, J. and van Haasteren, R., "Jellis18/PTMCMCSampler: Official Release." Zenodo (Oct. 2017).

[12] Levinstein, D. M., Sallum, S., Kim, Y. J., Lin, J., Lozi, J., Jovanovic, N., Fitzgerald, M. P., and Vievard, S., "Spectro-astrometry of embedded accreting protoplanets using photonic lanterns," in [*Techniques and Instrumentation for Detection of Exoplanets XI*], **12680**, 167–178, SPIE (Oct. 2023).

[13] Kim, Y. J., Fitzgerald, M. P., Lin, J., Sallum, S., Xin, Y., Jovanovic, N., Leon-Saval, S., Betters, C., Gatkine, P., Guyon, O., Lozi, J., Mawet, D., Norris, B., and Vievard, S., "Spectroastrometry and Imaging Science with Photonic Lanterns on Extremely Large Telescopes," (2023).

[14] Por, E. H., Haffert, S. Y., Radhakrishnan, V. M., Doelman, D. S., Van Kooten, M., and Bos, S. P., "High Contrast Imaging for Python (HCIPy): An open-source adaptive optics and coronagraph simulator," in [*Adaptive Optics Systems VI*], *Proc. SPIE* **10703** (2018).

[15] Kim, Y. J., Fitzgerald, M. P., Lin, J., Sallum, S., Xin, Y., Jovanovic, N., and Leon-Saval, S., "Coherent Imaging with Photonic Lanterns," *The Astrophysical Journal* **964**, 113 (Mar. 2024).

[16] Gullbring, E., Hartmann, L., Briceño, C., and Calvet, N., "Disk Accretion Rates for T Tauri Stars*," *The Astrophysical Journal* **492**, 323 (Jan. 1998).